Chinese Chemical Letters 35 (2024) 108922

Contents lists available at ScienceDirect

Chinese Chemical Letters

journal homepage: www.elsevier.com/locate/cclet

Epitaxial growth of $Cu_{2-x}Se$ on Cu (220) crystal plane as high property anode for sodium storage

Zhijia Zhang[a,*], Shihao Sun[a], Yuefang Chen[a], Yanhao Wei[a], Mengmeng Zhang[a], Chunsheng Li[b,c,*], Yan Sun[b,c], Shaofei Zhang[d,*], Yong Jiang[a]

[a] School of Materials Science and Engineering, Institute of Quantum Materials and Devices, State Key Laboratory of Separation Membrane and Membrane Processes, Tiangong University, Tianjin 300387, China
[b] School of Chemistry and Life Sciences, Suzhou University of Science and Technology, Suzhou 215009, China
[c] Key Laboratory of Advanced Electrode Materials for Novel Solar Cells for Petroleum and Chemical Industry of China, Suzhou University of Science and Technology, Suzhou 215009, China
[d] Hebei Key Laboratory of Flexible Functional Materials/Hebei Key Laboratory of Material Near-Net Forming Technology, School of Materials Science and Engineering, Hebei University of Science and Technology, Shijiazhuang 050018, China

ARTICLE INFO

Article history:
Received 27 July 2023
Revised 2 August 2023
Accepted 9 August 2023
Available online 10 August 2023

Keywords:
Cu2se
3D architecture
Anode materials
Density functional theory calculation
Sodium-ion battery

ABSTRACT

Three-dimentional (3D) transition metal selenides with sufficient channels could produce significant superiority on enhancing reaction kinetics for sodium-ion batteries. However, the thorough exploration of 3D architecture with a facile strategy is still challenging. Here we report that a polycrystalline $Cu_{2-x}Se$ film was epitaxial grown on (220) facets-exposed Cu by direct selenization of a nanoporous Cu skeleton, which is obtained by dealloying rolled CuMn@Cu alloy foil. Density functional theory calculation result shows strong adsorption energy for Se atoms on Cu (220) planes during selenization reaction, rendering a low energy consumption. By virtue of this core-shell 3D nanoporous architecture to offer abundant active sites and endow fast electron/ion transportation, the nanoporous $Cu_{2-x}Se$@Cu-0.15 composite electrode exhibits remarkable sodium-ion storage properties with high reversible capacity of 950.6 μAh/cm^2 at 50 μA/cm^2, suprior rate capability of 457.6 μAh/cm^2 at 500 μA/cm^2, as well as an ultra-long stability at a high current density. Mechanism investigation reveals that the electrochemical reaction is a typical conversion-type reaction with different intermediates. This novel electrode synthetic strategy provides useful instructions to design the high-performance anode material for sodium-ion batteries.

Resource shortage of lithium is becoming a major issue that will impede the development of energy storage devices [1–3]. Inspired by the similar physicochemical properties with lithium, sodium (Na) has aroused strong research interest in the application of Na-ion battery (SIB) [4–8]. The practical feasibility of SIBs, however, is still limited by the sluggish reaction kinetics and poor cycling stability, mainly attributes to repeated insertion/extraction of high radius Na^+ (1.02 Å) together with serious structural collapse of the electrodes [9–11]. Hard carbon as a primary anode material has been implemented in industrial area, while the low specific capacity (around 350 mAh/g) cannot meet the high-energy-density requirement [12–14]. Hence, developing alternative anode materials with high theoretical capacity, fast reaction kinetics and excellent cyclic stability are benefit for the advancement of SIBs but still challenging [15,16].

Regarding reported anode candidates, transition metal chalcogenides (TMCs) with merits of tailored morphology and multitudinous charge storage mechanism are greatly popular as promising alternatives to hard carbon [17–19]. Among various TMCs anodes, metal selenides, especially for copper selenide, can reserve Na^+ through both intercalation and multiple electron conversion mechanism. It means that it can produce high reversible specific capacities [20]. For example, Xu *et al.* designed a Cu_2Se electrode by selenizing metal-organic frameworks (MOF) [21]. It delivered a high reversible specific capacity of 207 mAh/g at the current density of 1.0 A/g. To further improve the electrochemical performance, Xiao *et al.* prepared a porous Cu_2Se architecture with high capacity of 426 mAh/g at 0.1 A/g, and high capacity retention of 90% at a current density of 20 A/g [22]. However, the critical issues including the poor electronic conductivity and sluggish surface ion transport are still pending.

* Corresponding authors.
E-mail addresses: zhangzhijia@tiangong.edu.cn (Z. Zhang), ichsheng@163.com (C. Li), zhangshaofei988403@163.com (S. Zhang).

https://doi.org/10.1016/j.cclet.2023.108922
1001-8417/

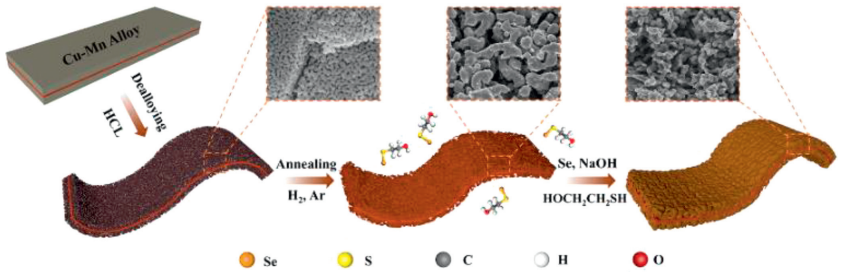

Fig. 1. Schematic representation of the preparation of copper process of the flexible $Cu_{2-x}Se$@Cu composite electrode.

Compared to Cu_2Se, the non-stoichiometric $Cu_{2-x}Se$ are rich in crystal defect [23]. The disorderly distributed Cu ions among Se atoms makes $Cu_{2-x}Se$ a p-type semiconductor, which provides much higher electronic conductivity than stoichiometric Cu_2Se. Furthermore, the larger space of the layered structure in $Cu_{2-x}Se$ could accommodate more Na^+, thus produce high reaction reversibility and fast kinetics. For example, Li *et al.* synthesized $Cu_{2-x}Se$ nanocrystals with mesoporous structure by solvothermal reaction. Benefitting from the mesoporous architecture and enriched defects, it could maintain a high specific capacity of 212.4 mAh/g at 5 A/g after 3000 cycles [24]. However, most of those $Cu_{2-x}Se$ materials were powder-like, which should be used by coating the mixture slurry (containing active materials, polymer binders and carbon black) on current collectors [25,26]. It can inevitably induce increased ohmic resistance and poor specific surface area properties [27,28]. For that matter, a free-standing $Cu_{2-x}Se$ electrode with nanoarchitectures is of great significance to solve above obstacles [29,30]. The specific surface area properties and reaction kinetics can be easily promoted by anchoring $Cu_{2-x}Se$ on a free-standing and 3D conductive enhancement, especially in a thick electrode. Yet issues arise in thick electrode design because of prolonged diffusion distances and poor mechanical stability [31,32]. Therefore, there is also an urgent demand to develop integrated 3D $Cu_{2-x}Se$ anodes by a simple preparation process for high-energy SIBs.

In this paper, the sandwich-like nanoporous $Cu_{2-x}Se$@Cu thick electrode was *in situ* constructed by selenization treatment at room temperature based on flexible nanoporous Cu skeleton, which was fully exposed (220) crystal surface during dealloying CuMn/Cu/CuMn process. Density functional theory (DFT) calculation result verifies that the adsorption energy of Se atoms on Cu(220) plane is stronger than that of on Cu(111) plane. Such a 3D nanoporous architecture not only provides abundant active sites and mechanical stability, but also accelerates reaction kinetics, resulting in advanced electrochemical properties in SIBs. The optimized $Cu_{2-x}Se$@Cu-0.15 composite electrode shows high areal specific capacities of 950.6 μAh/cm^2 at 50 μA/cm^2. Meanwhile, the $Cu_{2-x}Se$@Cu-0.15 electrode displayed a long-term stability of 457.6 μAh/cm^2 over 500 cycles at 500 μA/cm^2. This work highlights scientific insights for the exploration of metal selenides by a facile method for SIB.

Fig. 1 shows the preparation process for the flexible $Cu_{2-x}Se$@Cu composite electrode, involving the successive dealloying, annealing and selenation. XRD was first used to analyze the phases evolution from CuMn@Cu alloy to $Cu_{2-x}Se$@Cu electrode (Fig. S1 in Supporting information). After carrying out dealloying, the alloy peaks in NPA-Cu shift to right obviously with peaks location at 43.32°, 50.45° and 74.12° due to the absolutely dissolution of Mn, and can be ascribed as fcc structural Cu (JCPDF No. 04–0836) (111), (200) and (220) planes. In H–NPA-Cu sample, the peaks represented as Cu are well-crystallized because of heat annealing. Noteworthy, the H–NPA-Cu has an obvious preferred orientation, and more (220) crystal planes are exposed. The Rietveld refinement result (Fig. S2 in Supporting information) was employed, and the calculated R_{wp} value is as low as 4.61%. The preferred orientation of H–NPA-Cu could be attributed to the texture generated by rolling the alloy. Since the previous studies demonstrated the activity of Cu can affect the selenidation process, the crystal facet modification on different Cu planes is revealed here. The hydroxyethylthioselenide, H–NPA-Cu (220) and Cu (111) crystal plane were used as models, and the adsorption energy of hydroxyethylthioselenide on different crystal planes were calculated by DFT using VASP. Figs. 2a and b show the optimized reaction paths of $HOCH_2CH_2SSe^-$ with H–NPA-Cu (220) and Cu (111) crystal planes, respectively. As shown in Fig. 2c, the calculated energies of intermediate complexes at step 2 are −1.97 eV and −3.26 eV for Cu (111) and H–NPA-Cu (220), respectively. Clearly, the H–NPA-Cu (220) crystal planes show stronger adsorption of $HOCH_2CH_2SSe^-$than Cu (111), which could accelerate the formation of intermediate complexes. The energy of the intermediate complex increases slightly when the transition state is formed, but the product energy is more negative than the intermediate complex, meaning that the reaction is still a spontaneous process. The product energy obtained by the reaction of hydroxyethylthioselenide with H–NPA-Cu (220) crystal plane is more negative, indicating that the product is in a more stable state of thermodynamics.

The XRD pattern of $Cu_{2-x}Se$@Cu was shown in Fig. 3a. The peaks at 2θ of 26.75°, 44.60°, 71.59°, and 88.39° are close to fcc Cu_2Se (JCPDS No. 88–2043), which can be indexed as (111), (220), (311) and (511) planes, respectively. It is worth noting that the peaks of Cu at 2θ of 42.87°, 49.98°, 73.20°, and 88.85° are shift to lower diffraction angles after selenidation, showing that the introduction of Se^{2-} increased the interplanar distance of Cu. The observation of $Cu_{2-x}Se$ and Cu verified the successful formation of Cu-core@$Cu_{2-x}Se$-shell structure, which is benefit for enhancing electronic conductivity.

XPS was used to further characterize the elements valence distribution of $Cu_{2-x}Se$@Cu. Cu and Se signals were facilely observed in the XPS survey spectrum (Figs. 3b–d). Cu $2p_{3/2}$ and Cu $2p_{1/2}$ can be separately divided into two peaks. The peaks near at 932.62 and 952.34 eV could be ascribed to Cu^+ $2p_{3/2}$ and $Cu^+2p_{1/2}$, respectively. While the peaks located at 934.40 and 954.17 eV are corresponded to Cu^{2+} $2p_{3/2}$ and Cu^+ $2p_{1/2}$. Furthermore, the peaks at 940.71 eV, 943.48 eV, and 962.15 eV are confirmed as characteristic satellite peaks of Cu^{2+}. The peaks with binding energy located at 53.96 eV and 54.76 eV can be indexed as Se^{2-} 3d5/2 and Se^{2-} 3d3/2, respectively (Fig. 3d). A broad and weak peak at 58.79 eV is observed, which is originated from the surface oxidation of Se species. The absence of Cu^0 and Se^0 indicates that the Cu ligament was fully covered by $Cu_{2-x}Se$.

The microscopic morphology and structural evolution of the nanoporous anode was observed by SEM. Due to the desolution of Mn from CuMn layer, the NPA-Cu shows a bicontinuous nanoporous structure with pore size distributing near at 50 nm (Figs. S3a and c in Supporting information). To accelerate the infiltration of the reaction solution and favor the homogeneous growth

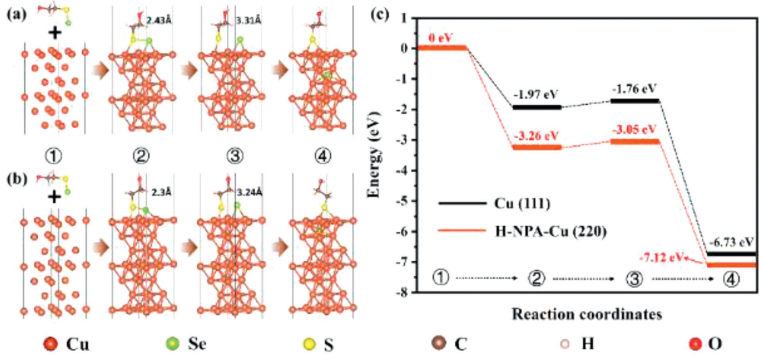

Fig. 2. Configurations of four different stages *in-situ* selenization process: (a) Cu (111), (b) H–NPA-Cu (220). (c) Energy profiles for reactions of $CH_2OHCH_2SSe^-$ with Cu (111) and H–NPA-Cu (220).

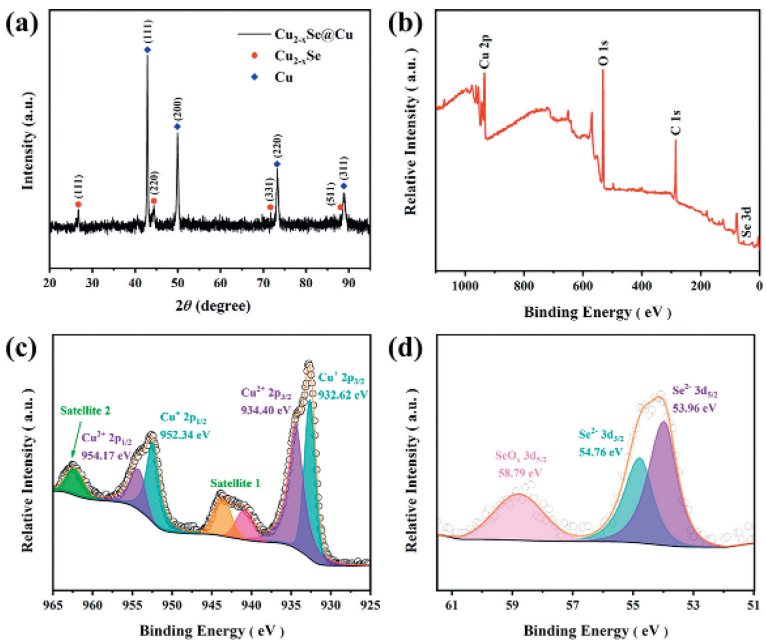

Fig. 3. (a) XRD pattern of $Cu_{2-x}Se$@Cu composite electrode. XPS spectra of $Cu_{2-x}Se$@Cu composite electrode: (b) Full survey, (c) Cu 2p, and (d) Se 3d.

of $Cu_{2-x}Se$ on the whole ligament, we further caried out annealing treatment to broaden the pore/ligament size. As shown in Figs. S3b and d (Supporting information), the pore size is expanded to around 500 nm, and the copper ligament is coarsened to about 700 nm. The pore size distribution tested in BET is consistent with the SEM results (Fig. S4 in Supporting information). Fig. 4a shows the cross-section morphology of the $Cu_{2-x}Se$@Cu composite electrode with thickness of ~100 μm. The loose layer above and below Cu foil could still be seen, indicating its integrity after *in-situ* growth of $Cu_{2-x}Se$. The copper foil act as not only current collector to enhance the electronic conductivity but also as supporter (Fig. 4a). The $Cu_{2-x}Se$@Cu composite electrode inherited good flexibility and mechanical stability from NPA-Cu (Fig. 4a and Fig. S5a in Supporting information) or H–NPA-Cu (Fig. S5b in Supporting information). The high-resolution SEM images of $Cu_{2-x}Se$@Cu composite electrode are shown in Figs. 4b and c. Compared to H–NPA-Cu sample, the pore size became slightly smaller and the surface became rougher, caused by the *in-situ* growth of $Cu_{2-x}Se$. The surface morphologies of the $Cu_{2-x}Se$@Cu composite electrodes with Se mole proportion of 0.05, 0.1, and 0.15 ($Cu_{2-x}Se$@Cu-0.05/0.1/0.15) are shown in Fig. S6 (Supporting information). Clearly, the $Cu_{2-x}Se$ species exhibited spherical shape with differentiate particle size distributions. It exhibits a loose dense distribution of $Cu_{2-x}Se$

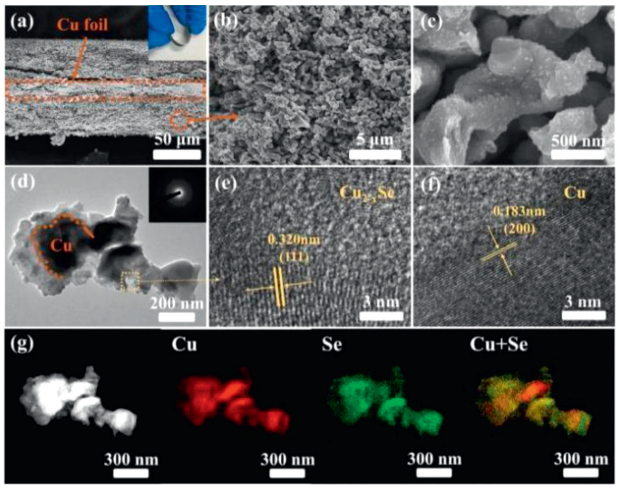

Fig. 4. SEM image of $Cu_{2-x}Se$@Cu composite electrode: (a) Cross section (optical image is shown in the inset); (b, c) Amplification diagram of cross section. TEM $Cu_{2-x}Se$@Cu composite electrode; (d) Low-resolution image; (e, f) HRTEM image; (g) EDS maps of the Cu and Se distributions.

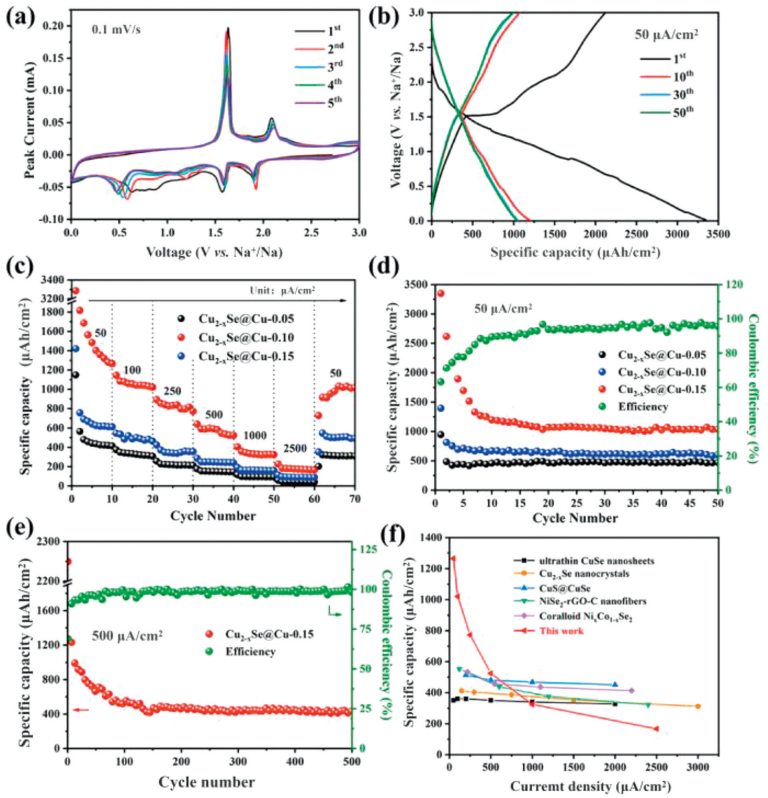

Fig. 5. Electrochemical performance for $Cu_{2-x}Se$@Cu composite electrode in SIBs: (a) CV curves and (b) galvanostatic charge-discharge profiles of $Cu_{2-x}Se$@Cu-0.15. (c) Rate capability and (d) cycling performance of $Cu_{2-x}Se$@Cu-0.05/0.1/0.15 electrodes. (e) Long cycling performance and (f) capacity comparison of the $Cu_{2-x}Se$@Cu-0.15 electrodes.

spheres (~1 μm) for $Cu_{2-x}Se$@Cu-0.05 sample. Then the particle reduces to smaller sizes along with increase the proportion of Se (600 nm for $Cu_{2-x}Se$@Cu-1.5). In addition, the Se content inside the $Cu_{2-x}Se$@Cu anodes with three different ratios was characterized by EDX (Figs. S7a–c in Supporting information), and the internal selenium content increases apparently along with the increasement of Se during selenidation process.

The microstructure of the $Cu_{2-x}Se$@Cu-1.5 composite electrode was further characterized by TEM. Fig. 4d shows that the Cu ligament is surrounded by $Cu_{2-x}Se$ (~80 nm). The selected area electron diffraction (SAED) pattern (insert of Fig. 4d) with diffraction rings manifests that $Cu_{2-x}Se$@Cu is a mixed polycrystalline structure. The interplanar spacings of 0.320 (Fig. 4e) and 0.183 nm (Fig. 4f) in high-resolution TEM images could be ascribe to the (220) crystal plane of $Cu_{2-x}Se$ and (200) crystal plane of Cu, respectively. The high-angle annular dark field (HAADF) image with its compositional mappings of Cu and Se (Fig. 4g) depict the homogeneous distribution of Se and Cu with a typical core shell structure.

The electrochemical performance of flexible $Cu_{2-x}Se$@Cu anodes are revealed by assembling CR2032 half-cells. Firstly, the sodium-ion storage behavior of the $Cu_{2-x}Se$@Cu-0.15 composite electrode was investigated using CV at scan rate of 0.1 mV/s (Fig. 5a). In the first discharge process, the two peaks around 1.89 V and 1.57 V, corresponding to the insertion of Na^+ into $Cu_{2-x}Se$ lattice with the formation of Cu and Na_xCuSe phases. The broad peak at 0.62 V maybe caused by the complete conversion of Na_xCuSe to Na_2Se, the SEI film formation. In the initial anodic scan, the intense anodic peaks could be observed at 1.62, 1.84 and 2.09 V, which respectively corresponds to the conversion of Na_2Se and Cu to Na_xCuSe and $Cu_{2-x}Se$ alloy step by steps. In the following scans, the CV patterns display the same tendency and almost completely overlap, illustrating that the conversion reaction is reversible and the stability is good. Fig. 5b shows the galvanostatic charge-discharge profiles of $Cu_{2-x}Se$@Cu-0.15 with 50 μA/cm² from the 1st to 50th. All detected charge-discharge plateaus could well correspond to the redox peaks in the CV curves, proving a multistep conversion reaction.

The cycle and rate performance of $Cu_{2-x}Se$@Cu-0.05/0.1/0.15 electrodes are also performed in this work. The discharge area specific capacities of $Cu_{2-x}Se$@Cu-0.15 electrode are 950.6, 868.3, 701.6, 511.1, 370.4, and 217.6 μAh/cm² at current densities of 50, 100, 250, 500, 1000, and 2500 μA/cm², respectively, which were significantly superior to $Cu_{2-x}Se$@Cu-0.05 and $Cu_{2-x}Se$@Cu-0.1 electrodes (Fig. 5c). When the current density returned to 50 μA/cm², the capacity could be maintained at 762.6 μAh/cm², demonstrating an outstanding reversibility. The $Cu_{2-x}Se$@Cu-0.05 and $Cu_{2-x}Se$@Cu-0.1 electrodes exhibit a discharge area specific capacity of 472.4 μAh/cm² and 601.7 μAh/cm² after 50 cycles, respectively (Fig. 5d). In comparison, the specific area capacity of $Cu_{2-x}Se$@Cu-0.15 could achieve 754.2 μAh/cm². Even at 500 μA/cm², $Cu_{2-x}Se$@Cu-1.5 anode could still maintains the highest reversible capacity of 322 μAh/cm² after 500 cycles, better than $Cu_{2-x}Se$@Cu-0.05 (143.4 μAh/cm²) and $Cu_{2-x}Se$@Cu-0.10 (200.5 μAh/cm²) anodes (Fig. 5e). The microstructure of $Cu_{2-x}Se$@Cu-0.15 electrode after 500 cycles was further characterized by SEM (Fig. S8 in Supporting information). The dense $Cu_{2-x}Se$ layer on the electrode surface disappeared well and exposed more channels, comparing to the initial sample, so that the electrolyte can smoothly enter the deep of electrode. The internal bicontinuous nanoporous structure of the $Cu_{2-x}Se$@Cu-0.15 electrode is extremely stable (Fig. S8a). Compared with similar electrodes, $Cu_{2-x}Se$@Cu-0.15 anode exhibits higher energy density, especially under low current conditions (Fig. 5f).The high performance of $Cu_{2-x}Se$@Cu-0.15 is owing to both of intrinsic nature of $Cu_{2-x}Se$ and high stable nanoporous framework, which facilitates the Na^+ diffusion.

The electrochemical behavior was evaluated by kinetic investigation to further understand the high performance of $Cu_{2-x}Se$@Cu-0.15 electrode (Figs. S9a–d in Supporting information). The currents increase and potentials slightly shift with the increasing scan rates from 0.1 mV/s to 1 mV/s, illustrating fast charges and ions diffusion in $Cu_{2-x}Se$@Cu electrode. In SIBs, the diffusion-controlled process (battery behavior) and pseudocapacitive-controlled process (capacitive behavior) determines the Na^+ charge storage capacity. The capacitive contribution increases apparently from 53% to 91.05%, demonstrating the excellent ion accessibility (Figs. S9c and d in Supporting information). The high-rate performance could be ascribed to the bicontinuous nanoporous structure.

The electrochemical impedance spectroscopy (EIS) was further investigated with the electrode charged to 1.6 V after 5 cycles (Figs. S9e and f in Supporting information). The Nyquist plots present two semicircles, corresponding to the resistance of Na^+ diffusion through the SEI film (R_f) and charge-transfer resistance (R_{ct}), respectively. In addition, the ohmic resistance (R_s), containing separator paper resistance and electrode resistance, is only 6.7 Ω. The equivalent circuit is shown in insert image of Fig. S9e. The fitted result shows that $Cu_{2-x}Se$@Cu-0.15 exhibited a lower R_{ct} of 257.4 Ω than $Cu_{2-x}Se$@Cu-0.05 (384.5 Ω) and $Cu_{2-x}Se$@Cu-0.1 (530.6 Ω). Benefiting from the unique nanoporous skeleton, the charge transfer resistance can be reduced and Na^+ transfer efficiency can be enhanced in the $Cu_{2-x}Se$@Cu-0.15 composite electrode.

In summary, we introduce a facile strategy to *in-situ* grow $Cu_{2-x}Se$ on (220) facets-exposed Cu by direct selenization of a nanoporous Cu skeleton. The $Cu_{2-x}Se$@Cu-0.15 anode possessed excellent electrochemical properties, including high reversible capacity of 950.6 μAh/cm^2 at 50 μA/cm^2. The high electrochemical properties attribute to the following factors: Firstly, the sandwiched Cu can synergy with nanoporous Cu skeleton to enhance the electronic conductivity and maintain the material integrity; Secondly, the nanoporous $Cu_{2-x}Se$ frameworks on both sides provide sufficient spaces to accommodate Na^+ diffusion. This novel strategy provides a new way to synthesize the flexible integrated electrodes with high storage capacity for sodium ions.

Declaration of competing interest

The authors declare that they have no known competing financial interests or personal relationships that could have appeared to influence the work reported in this paper.

Acknowledgments

This work was financially supported by the National Natural Science Foundation of China (Nos. 52271011, 52102291, 52101251). We would like to thank the Analytical & Testing Center of Tiangong University for Transmission Electron Microscope work.

Supplementary materials

Supplementary material associated with this article can be found, in the online version, at doi:10.1016/j.cclet.2023.108922.

References

[1] T. Nagaura, J. Li, J.F. Fernando, et al., Small 18 (2022) 2106629.
[2] Z. Zhang, J. Zhao, Z. Qiao, et al., Rare Met. 40 (2021) 393–399.
[3] C. Li, Z. Zhang, Y. Chen, et al., Adv. Sci. 9 (2022) 2104780.
[4] J. Gou, Z. Qiao, Z. Yu, et al., Surf. Innov. 11 (2022) 70–78.
[5] Z. Hao, X. Shi, Z. Yang, et al., Adv. Funct. Mater. 32 (2022) 2208093.
[6] X. Peng, Y. Yan, S. Xiong, et al., J Mater. Sci. Technol. 118 (2022) 136–143.
[7] Z. Zhang, Y. Chen, S. Sun, et al., J Mater. Sci. Technol. 119 (2022) 167–181.
[8] S. Sun, Z. Zhang, L. Yan, et al., J Porous Mater. 29 (2022) 249–255.
[9] L. Yue, D. Wang, Z. Wu, et al., Chem. Eng. J. 433 (2022) 134477.
[10] X. Li, X. Sun, X. Hu, et al., Nano Energy 77 (2020) 105143.
[11] N.T. Aristote, K. Zou, A. Di, et al., Chin. Chem. Lett. 33 (2022) 730–742.
[12] X. Chen, M. Li, S.P. Wang, et al., Adv. Sci. 9 (2022) 2104630.
[13] Z. Zhang, G. Xie, Y. Chen, J Mater. Sci. Technol. 171 (2024) 16–23.
[14] X. Ma, Z. Zhang, J. Wang, et al., Rare Met. 40 (2021) 2802–2809.
[15] H. Li, X. Zhang, Z. Zhao, et al., Energy Storage Mater. 26 (2020) 83–104.
[16] Y. Fang, L. Xiao, Z. Chen, et al., Electrochem. Energy Rev. 1 (2018) 294–323.
[17] Z. Yu, Q. Sun, H. Li, et al., Rare Met. 42 (2023) 2982–2992.
[18] Y. Cai, P. Du, Y. Huang, ACS Appl. Nano Mater. 5 (2022) 15692–15699.
[19] Q. Pan, M. Zhang, L. Zhang, et al., ACS Nano 14 (2020) 17683–17692.
[20] M. Luo, H. Yu, F. Hu, et al., Chem. Eng. J. 380 (2020) 122557.
[21] X. Xu, J. Liu, J. Liu, et al., Adv. Funct. Mater. 28 (2018) 1707573.
[22] Y. Xiao, X. Zhao, X. Wang, et al., Adv. Energy Mater. 10 (2020) 2000666.
[23] Q. Gao, P. Li, S. Ding, et al., Ionics 26 (2020) 5525–5533.
[24] Y. Li, X. Sun, Z. Cheng, et al., Energy Storage Mater. 22 (2019) 275–283.
[25] Z.Y. Gu, Z.H. Sun, J.Z. Guo, et al., ACS Appl. Mater. Interfaces 12 (2020) 47580–47589.
[26] J.L. Zhang, C.L. Li, W.H. Wang, et al., Rare Met. 40 (2021) 3460–3465.
[27] J. Wang, Z. Zhang, S. Sun, et al., Surf. Innov. 9 (2020) 207–213.
[28] L. Shao, S. Wang, J. Qi, et al., Mater. Today Phys. 19 (2021) 100422.
[29] X. Zhu, J. Gao, J. Li, et al., Energy Fuels 4 (2020) 2453–2461.
[30] H. Yang, S. Zhou, B.W. Zhang, et al., Adv. Funct. Mater. 31 (2021) 2102280.
[31] X. Li, N. Zhang, Y. Wu, et al., Rare Met. 41 (2022) 3401–3411.
[32] H. Yang, Z. Zhang, Z. Yu, et al., Mater. Lab 1 (2022) 220016.